

Quantum Oscillations in iron-doped topological insulator Sb_2Te_3 crystals

Weyao Zhao^a, David Cortie^{a,b}, Lei Chen^a, Zhi Li^{a,b}, Zengji Yue^{a,b}, and Xiaolin Wang^{a,b*}

^a *Institute for Superconducting and Electronic Materials, Australian Institute for Innovative Materials, University of Wollongong, NSW 2500, Australia*

^b *ARC Centre of Excellence in Future Low-Energy Electronics Technologies FLEET*

Abstract: We investigated the magnetotransport properties of Fe-doped topological insulator $\text{Sb}_{1.96}\text{Fe}_{0.04}\text{Te}_3$ single crystals. With doping, the band structure changes significantly and multiple Fermi pockets become evident in the Shubnikov-de Haas oscillations, in contrast to the single frequency detected for pure Sb_2Te_3 . Using complementary density functional theory calculations, we identify an additional bulk hole pocket introduced at the Γ point which originates from the chemical distortion associated with the Fe-dopant. Experimentally, both doped and undoped samples are hole-carrier dominated, however, Fe doping also reduces the carrier density and mobility. The angle dependent quantum oscillations were analyzed to characterize the complex Fermi surface and isolate the dimensionality of each SdH feature. Among the components, at least two pockets possess 2D-like behavior according to their rotational dependence. These results indicate a complex interplay of hybridized dopant bands with the bulk and surface topological electronic structure.

*Corresponding author: xiaolin@uow.edu.au

1. Introduction

Topological insulators (TIs) are materials with a symmetry-protected non-trivial electronic structure which can yield an insulating bulk with conducting boundaries. The emergent Dirac surface states are attractive for electronic applications and potentially host a range of fascinating phenomena including the quantum spin Hall effect, topological magnetoelectric effect, magnetic monopole images and Majorana fermions.[1-4] In 3D topological insulators such as the (Bi,Sb)₂Te₃ family, the surface electronic structure is entangled with the bulk electronic structure, and consequently, both aspects need to be understood at the fundamental level. Currently, there are a number of unresolved questions concerning the effect of transition metal doping in the (Bi,Sb)Te₃ family and this is related to one of the most fascinating transport properties in the TIs, namely the quantum anomalous Hall effect (QAHE). Shortly after it was predicted [5], the QAHE was experimentally realized in doped (Bi,Sb)₂Te₃[6] thin films. The Hall resistance reaches the predicted quantized value of h/e^2 , accompanied by a considerable drop in the longitudinal resistance[6], which would significantly reduce the power consumption in electronic devices. However, the onset temperature remains low, and it is widely believed that in-gap features are introduced by the transition metal dopant that are detrimental to performance. Therefore, magnetic doped TIs, e.g., V-, Cr- and Mn Sb₂Te₃[7-10], Fe- and Mn-doped single crystals of Bi₂Te₃[11, 12] and Cr-, Mn-doped of Bi₂Se₃[13, 14], are being increasingly studied to determine the optimal set of dopants, magnetic order and transport properties in thin films and single crystals. In this work, we report the electronic effects of doping Sb₂Te₃ single crystals with iron studied with magnetotransport experiments and complementary *ab initio* calculations.

Sb₂Te₃ has a tetradymite crystal structure, which belongs to the $R\bar{3}m$ space group, with quintuple (Te-Sb-Te-Sb-Te) layers piled up along the *c*-axis via the van de Waals interaction. As the ionic radii of the Sb³⁺ is very similar to a number of transition metals ($R(\text{Sb}^{3+}) = 0.76 \text{ \AA}$)[15] it is reasonable to expect efficient transition metal doping in this

family in contrast to Bi_2Te_3 where a larger mismatch occurs. Another potential advantage of Sb_2Te_3 is that the chemistry ratio of Sb:Te can be controlled by the growth process. By increasing Te pressure, the typical Te vacancies in single crystal Sb_2Te_3 can be reduced, which, remarkably, also depletes the bulk conduction channels, thus reducing the carrier density. In tandem, this increases the carrier mobility, e.g. mobilities as high as $25000 \text{ cm}^2\text{V}^{-1}\text{s}^{-1}$ have been attained, which are the highest for any of the existing topological materials[16]. We note that a past DFT study on the transition-metal doped 3D TIs predicts the Fe dopant is unique amongst the potential transition metal dopants because it is predicted to contribute to the density of states and result in multiple electron or hole pockets at the Fermi level in Fe doped Sb_2Te_3 . [17] This would be very interesting as the Fe doping is likely to have multiple effects by: 1) introducing a ferromagnetic or paramagnetic state; 2) tuning both types and density of charge carrier; 3) modifying the non-trivial transport state due to the intrinsic strong spin-orbit coupling in the Sb_2Te_3 . However, to the best of our knowledge, there is an absence of experimental study for the Fe-doped Sb_2Te_3 system. This motivated us to investigate the Fe doping effect on the electronic structure of Sb_2Te_3 by performing quantum transport measurements.

2. Methods

2.1. Experimental

High-quality Sb_2Te_3 and $\text{Fe}_{0.04}\text{Sb}_{1.96}\text{Te}_3$ (FST) single crystals were grown by the melting and slow-cooling method. Briefly, high-purity stoichiometric amount ($\sim 12 \text{ g}$) of Fe, Sb and Te powder were sealed in a quartz tube as starting materials. The crystal growth was carried out in a vertical furnace using the following temperature procedures: i) Heating the mixed powders to completely melt ii) Cooling rapidly to slight above the melting point, iii) Slowly cooling down to room temperature to crystallize the sample. After growth, single crystal flakes with a typical size of $5 * 5 * 0.2 \text{ mm}^3$ could be easily exfoliated mechanically from the ingot. Naturally, single crystals prefer to cleave along

the [001] direction, resulting in the normal direction of these flakes being (001), as shown the inset photograph of **Fig. 1(b, c)**. The strong (00 l) ($l = 6, 9, 12, 15, 18$) diffraction peaks (**Fig. 1(b, c)**) indicate that the single crystal is a c -oriented crystal flake.

The electronic transport properties were measured by the standard four-probe method using a physical property measurement system (PPMS-14T, Quantum Design). Ohmic contacts were prepared on a fresh cleavage ab plane using room-temperature cured silver paste. The electric current is parallel to the hexagonal ab plane while the magnetic field is orientated along the c -axis. Angle-dependent magnetoresistance (MR) was also measured using a standard horizontal rotational rig mounted on the PPMS.

2.2. Theoretical

Density Functional Theory (DFT) calculations were carried out using the plane-wave code, Vienna Ab-initio Simulation Package (VASP) version 5.44.[18, 19] The Generalized-Gradient Approximation using the Perdew–Burke–Ernzerhof (PBE) exchange-correlation functional was employed, together with the spin orbit interaction and Hubbard correction for the Fe d levels. The Hubbard terms were taken as $U = 3$ eV and $J = 0.28$ to be consistent with recent work, although investigations were performed for a range of values and found to yield similar results. Both pure Sb_2Te_3 and $Sb_{2-x}Fe_xTe_3$ were simulated with identical levels of precision. For the $Sb_{2-x}Fe_xTe_3$, a $2 \times 2 \times 1$ supercell was constructed containing a single Fe atom within a total of 60 atoms. An energy cut-off and electronic convergence of 300 eV and 1.0×10^{-5} eV respectively. Forces were converged within 0.02 eV/Å. Dispersion corrections were included via the Grimme D3 method to account for van der Waals interactions[20]. A k -point mesh equivalent to a $16 \times 16 \times 2$ mesh in the hexagonal unit cell was adopted. For visualizing the Fermi surface, a grid of spacing 0.1 \AA^{-1} was constructed corresponding to $20 \times 20 \times 4$ in the unit cell, and values were interpolated between these points.

3. Results and Discussion

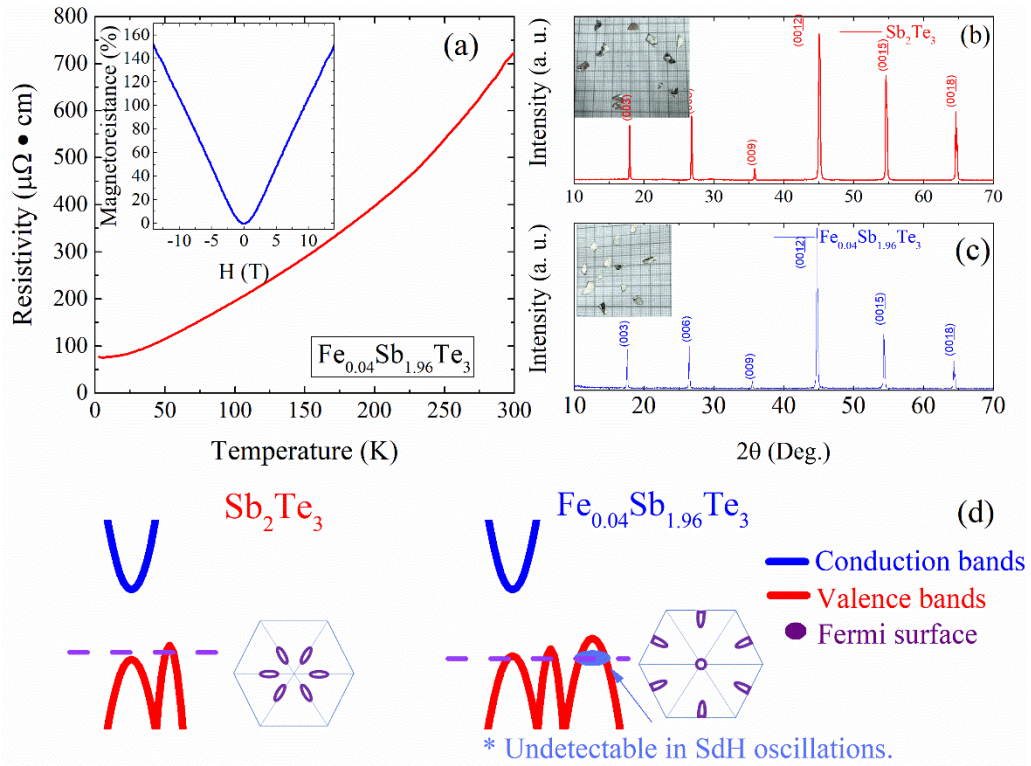


Fig. 1 (a) Resistivity of $\text{Fe}_{0.04}\text{Sb}_{1.96}\text{Te}_3$ as a function of temperature from 3 to 300 K. The inset shows the MR at 3 K up to 14 T. (b, c) the X-ray diffraction patterns of Sb_2Te_3 and FST single crystals along the c direction. The inset photos are crystal pieces cleave from the ingot. (d) Sketches of the band structure and Fermi surface of Sb_2Te_3 and FST.

Since the bonding between Sb and Te is relatively weak, it can lead to defects (e.g., Te vacancies) in the crystals, and this results in a metallic base state in Sb_2Te_3 [21]. This situation also occurs in our crystals. As shown in Fig. 2, the resistivity monotonically decreases with the cooling from 300 K to 3 K. At 3 K, the resistivity of FST is about $80 \mu\Omega\cdot\text{cm}$, presenting a good metallic state. Besides, the residual resistance ratio ($\text{RRR} = R(300 \text{ K})/R(3 \text{ K})$) is about 10, also indicating the good metallicity. The inset of Fig. 1 shows the magnetoresistance (MR), which defined by $(R(H) - R(0))/R(0)$, of FST single crystal with magnetic field perpendicular to the current. One can see the maximum MR value at 3 K is about 150%, similar to the MR previously studies in this system. Moreover, oscillations patterns could be found in the MR curve, attributed to the Shubnikov-de Haas (SdH) effect. The aforementioned XRD results, as well as the magneto- transport properties, demonstrate the good quality of as-grown single crystals.

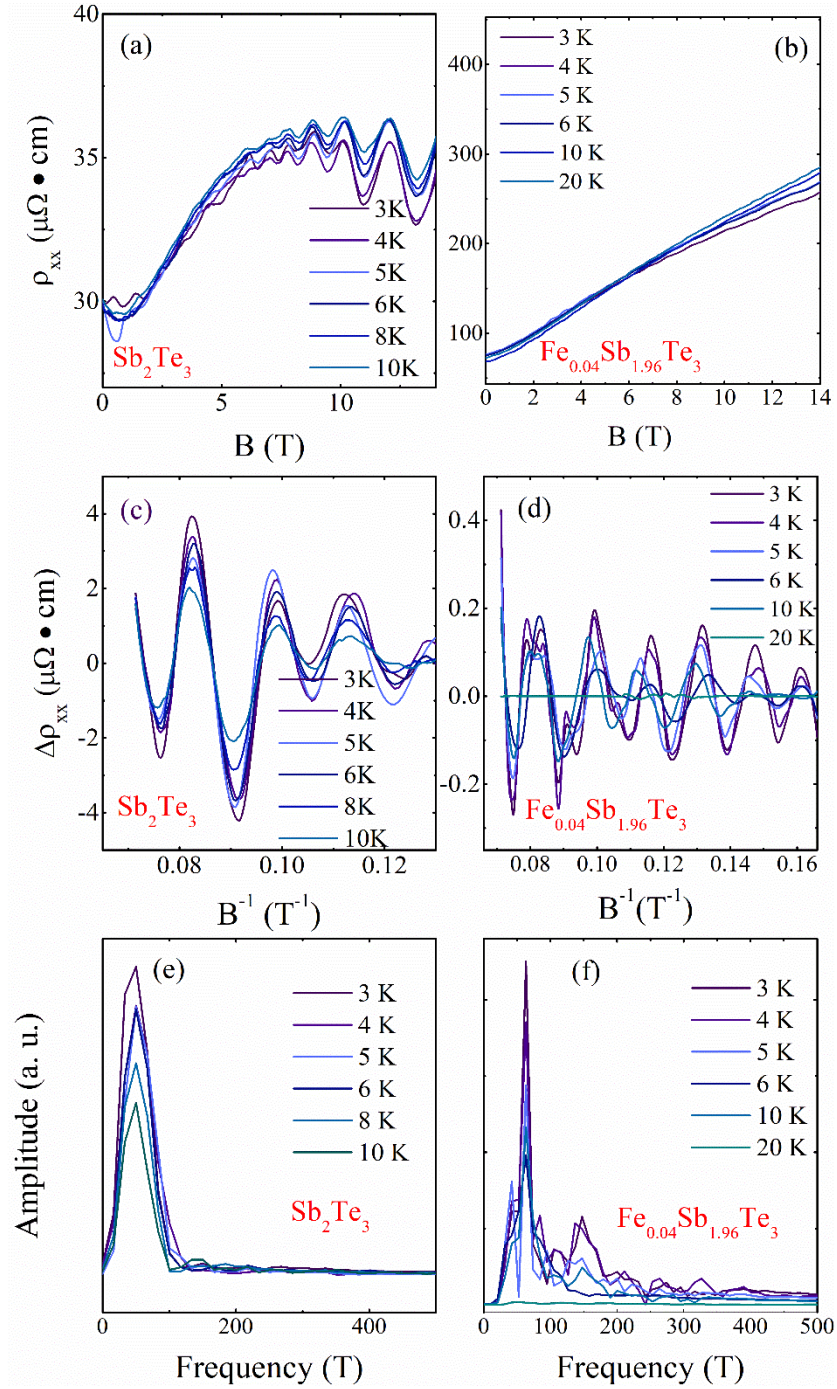


Fig. 2 SdH oscillations of both Sb_2Te_3 and FST single crystals. (a) and (b), MR curves of Sb_2Te_3 and FST single crystals measured at different temperatures; (c) and (d), oscillation patterns obtained by subtracting the smooth backgrounds at various temperatures, plotted as a function of $1/H$; (e) and (f), amplitudes of the the fast Fourier transform from the oscillations.

To further understand the SdH effect in Sb_2Te_3 and Fe-doped single crystals, we conducted a series of MR measurements at different temperatures shown in Fig. 2 (a)

and (b). In the pure Sb_2Te_3 crystals, the MR curves firstly increase with external magnetic fields, however, more-or-less saturate in above 8 T. The Fe-doped samples behaves significantly differently, resulting in a linear-like, unsaturated MR curves within the measured temperature range. The SdH oscillation amplitudes ($\Delta\rho = \rho - \langle\rho\rangle$) are obtained by subtracting a smooth non-oscillatory background $\langle\rho\rangle$ from the oscillating total resistivity (ρ). These are plotted against the inverse magnetic field in the Panel (e) and (f) of Fig. 2. The oscillation amplitude displays complex periodic behaviors and decreases with increasing temperature. It is noteworthy that the oscillation amplitude of Sb_2Te_3 is one order-of-magnitude larger than it in FST, which is taken to imply that there are additional defects induced by the doping process that contribute to charge-carrier scattering. In Panel (c) and (d), one can see the oscillation patterns are different from each other: while there is a single oscillatory mode in Sb_2Te_3 , numerous frequencies appear for the FST. To analyze, the oscillations, we performed fast Fourier transforms as shown in Panel (e) and (f). A single peak at ~ 50 T can be found in Sb_2Te_3 , indicating that a single pocket exists near the Fermi surface as shown in Fig. 1(d), which agrees well with the band structure calculation [4], and also the previous sdH experiments on p-type Sb_2Te_3 . [22]. Note that, the peak value decreases as the temperature increases. In the present study, multiple oscillation peaks with frequencies at about 62, 150 T, can be detected, representing the multiple large pockets at the Fermi surface shown in Fig. 1(d), which agrees with the DFT calculations, as discussed in a later section.

The oscillations frequency F is related to the cross section of the Fermi surface A , by the Onsager relation: $F = (h/2\pi e) \cdot A$; here, h is Plank's constant, e is the elementary charge. Therefore, the cross section of Sb_2Te_3 is 0.48 nm^2 , while in FST, more than one cross section can be detected with an area of 0.62 and 1.44 nm^2 , respectively. The relative Fermi wave vector K_F can be calculated as $K_F = (A/\pi)^{-2}$ giving 0.29 , 0.44 and 0.68 nm^{-1} . According to LK theory [23], $M_{os} \propto R_T R_D \sin(\frac{2\pi F}{B} + \beta)$, where M_{os} is the magnitude of oscillation, R_T is the temperature damping factor, R_D is the Dingle

damping factor and β is the Berry phase, respectively. The effective mass m^* can be extracted from the temperature dependence of the SdH oscillation amplitudes by $R_T = \frac{\alpha T m^*}{B \cdot \sinh(\alpha T m^*/B)}$, in which $\alpha = \frac{2\pi^2 k_B m_e}{eh} \sim 14.96$ T/K, where k_B is the Boltzmann constant and m_e is the electron rest mass. We fit the temperature dependence of SdH oscillation amplitude of Sb_2Te_3 and FST as shown in Fig. S₂, to obtain the effective masses are 0.23 and 0.37 m_e , respectively. The extrapolated Landau-level index ν at the extreme field limit, e.g., $1/B \rightarrow 0$, is related to Berry's phase, which indicates a phase shift regarding the conventional Landau quantization in materials. The intercept $\nu = 0$ corresponds to a normal metal, while $\nu = 0.5$ comes from the massless relativistic fermions in a magnetic field. As shown in Fig. S₂, the intercept of Sb_2Te_3 and FST single crystal are -0.5 and -0.3 (0.7), respectively, indicating that the quantum oscillations might be contributed by the surface states in Sb_2Te_3 , but are sensitive to a mixed contribution of surface states and bulk states in FST. The aforementioned parameters are summarized below in Table 1.

Sample	Frequency (T)	Area (nm ⁻²)	Fermi Vector (nm ⁻¹)	Effective Mass (m_e)	Berry Phase (2π)
Sb_2Te_3	50	0.48	0.29	0.23	0.5
FST	62	0.62	0.44	0.37	0.7
	150	1.44	0.68		

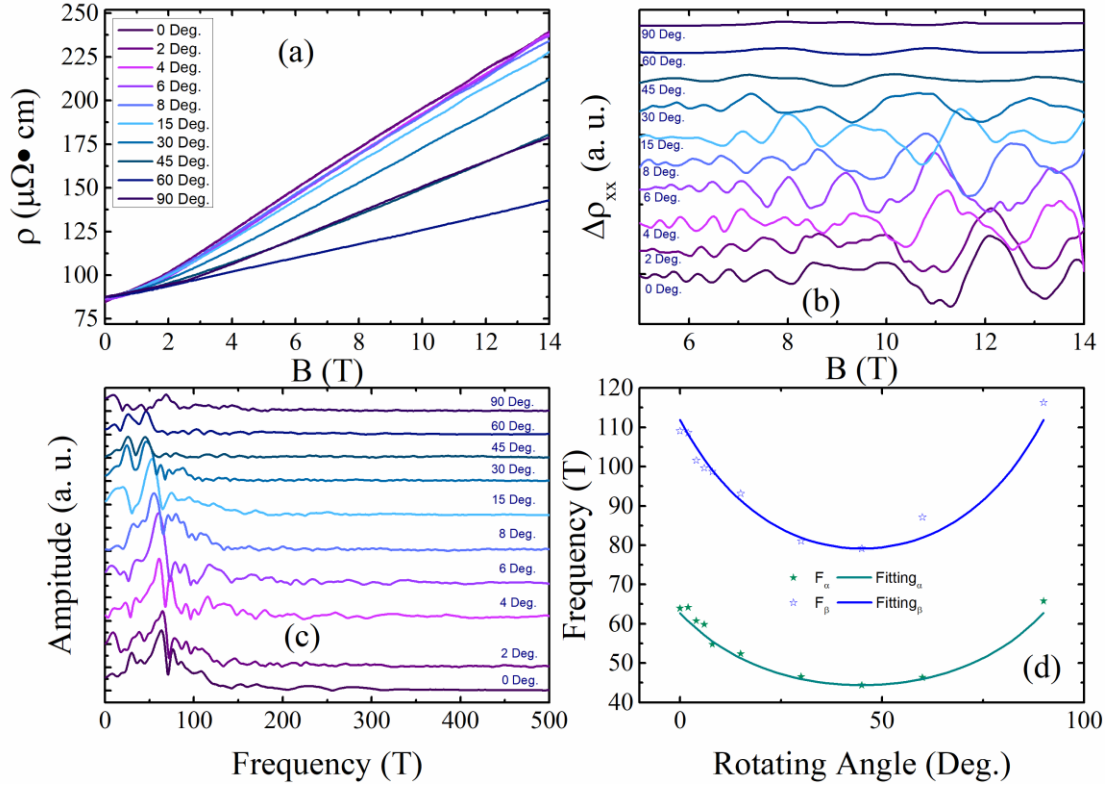


Fig. 4 Angular-dependence of the SdH oscillations of the FST single crystal. (a) MR curves of FST single crystals measured at different angles at 3 K; (b) oscillation patterns obtained by subtracting the smooth backgrounds at various angles, plotted as a function of B ; (c), amplitudes plots of fast Fourier transform from the oscillations; (d) two selected frequencies evolve with rotation, in which the star symbols are experimental data, while curves are fitted with $F(\theta)=F(0)/\cos(\theta-45)$.

The angle dependence of quantum oscillations at different tilt angles (θ) provides information about the shape, size and dimensionality of the Fermi surface. Fig. 4 shows the MR at different θ values. In the MR plot displayed in Fig. 4(a), the maximum resistivity value decreases in the rotation process and reaches the minimum value at 60 degrees. Interestingly, the MR value at 90 degrees, which means the external magnetic field is parallel to the current, is larger than that of 60 degrees. and comparable with the magnitude of 45 degrees. During the rotation towards 90 degrees., the oscillation component gradually weakens. After carefully subtracting the background, the oscillation pattern can be found at all positions, which are plotted as a function of H in Fig. 4(b) and $1/B$ in Fig. 4(c). Obviously, the positions of maxima and minima change

systematically with the tilt angle. Fig 4(c) shows the FFT of the quantum oscillations at various angles, showing the multi-frequency nature of FST single crystal at all angles. In Fig. 4(c), it is possible to observe that the frequency F in the rotating process decreases monotonically until 45 degrees., then increases. Since F is proportional to the cross section of the Fermi surface A , we conclude that A is not constant for different magnetic field orientations, which means the Fermi surface is not spherical but ellipsoid or some-other two dimensional like shape. We, therefore, fit the frequencies as a function of rotating angle in form of $F(\theta) = F(45)/\cos(\theta - 45)$. It is noted that the bulk valence band of Sb_2Te_3 is confirmed to consist of ellipsoidal valleys which are tilted by 45 degrees from the c axis [8]. Therefore, the oscillations may origin from the bulk state, due to the defects during single crystal growth, as well as the Fe doping. Together with the previously DFT calculation [6], we deduce the Fermi surface structure is close to the sketch in the inset of Fig. 1(d).

Moreover, the Landau-level index diagrams of oscillations from 0 to 30 Deg. are plotted in Fig. S3. Due to the multi-frequency nature of those oscillations, we chose one of the main patterns to determine the intercept. Interestingly, all of those intercepts are around -0.3 - -0.5, and are almost unchanging during the rotation process.

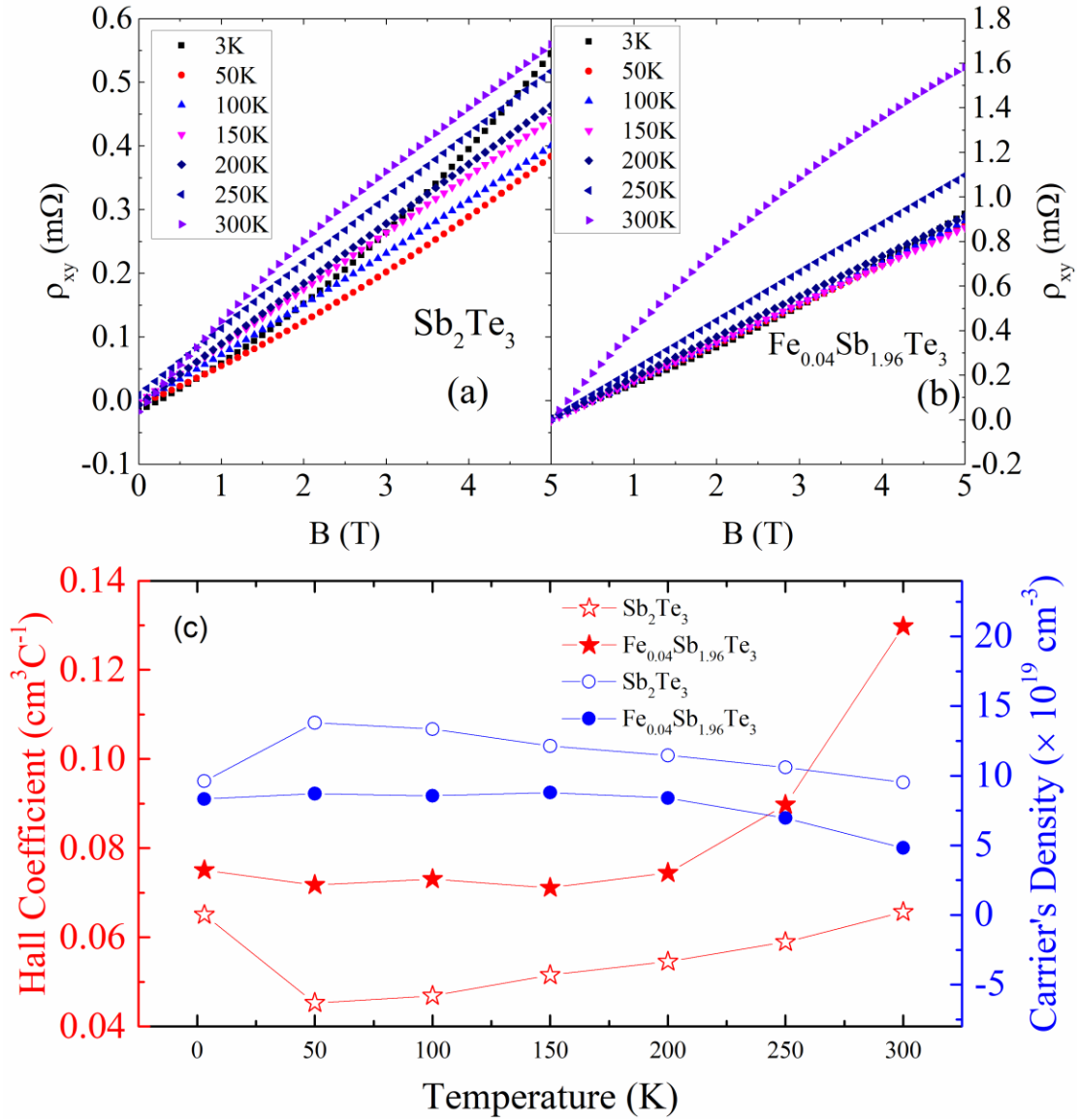


Fig. 5 Hall Effect of Sb_2Te_3 and FST single crystals. (a) and (b), ρ_{xy} plots of Sb_2Te_3 and FST single crystals at various temperatures. (c) The Hall coefficient and the carrier density calculated from the relative Hall curves are plotted as functions of temperature.

It is well known that the defects in Sb_2Te_3 contribute to the hole carriers, leading to a p-type semimetal. We here introduce Hall measurements to further verify this feature in our as grown Sb_2Te_3 single crystal, as well as check the effect of Fe doping. In Fig. 5 (a) and (b), the Hall Effect curves are plotted from 3 to 300 K. One can easily identify that the linear-like increasing curves, which correspond to a p-type conductor,

are contributed by hole carriers. Though past DFT calculations indicate that Fe doping may introduce electron carriers into Sb_2Te_3 [17], the curves are more likely corresponding to a single-hole carrier model, rather than a multi-carrier model.

At 3 K, the Hall coefficient of Sb_2Te_3 and FST are 0.065 and $0.075 \text{ cm}^3\text{C}^{-1}$, respectively. Together with the conductivity measured before, we can obtain the Hall mobility is $2167 \text{ cm}^2/\text{Vs}$ in Sb_2Te_3 and $990 \text{ cm}^2/\text{Vs}$ in FST. Fe-doping slightly reduces the carrier density and mobility of Sb_2Te_3 , while increasing the defect density. One possible reason is that Fe introduces electron carriers and might reduce the hole carriers contributed in Sb_2Te_3 . The carrier's density does not change much in the heating process, which might due to the carriers' origin from synthesis defects, not intrinsic carriers which evolves significantly with temperature.

Let us focus on the carrier density and mobility: the Fe dopant slightly reduces the carrier density, and significantly reduces the carrier mobility at 3 K. We attribute the doping effect on carriers to two general aspects: 1) Fe shifts the Fermi level towards the valence band, and thus increases the Fermi pocket area; 2) Fe introduces electron carriers, which might equally reduce the contribution of hole carriers in Hall measurements. Meanwhile, Fe dopant also introduces more defects in the crystal lattice, which may be one of the main reasons that reduce carrier's mobility in FST single crystal. Moreover, Fe dopant changes the Fermi surface morphology to a great extent: 1) more than two Fermi pockets appear in FST, compared to the single pocket in Sb_2Te_3 ; 2) the angle dependence measurements illustrates that those pockets possess a 2D or 2D-like shape. The relative complexity of the Fermi surface offers an an extra free degree of Fermi surface tuning, e.g., via thickness or gating.

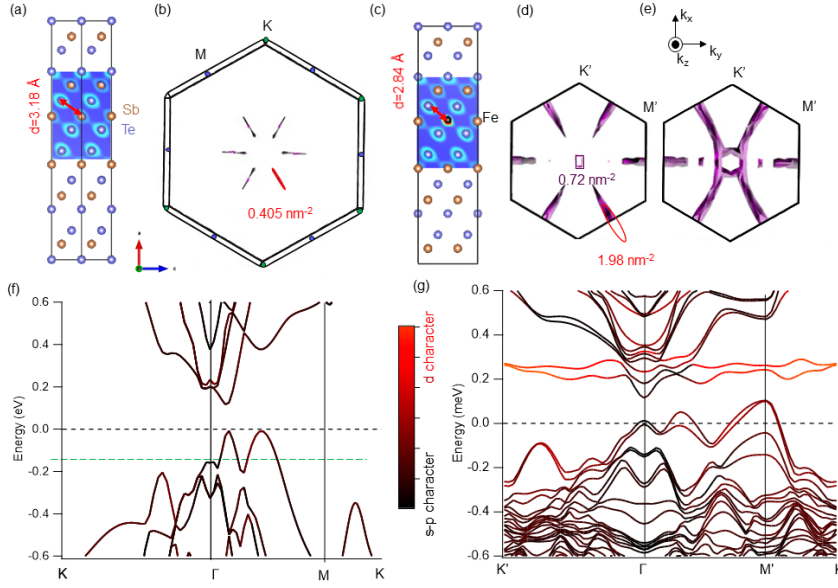


Fig. 6 DFT calculations for Sb_2Te_3 and $\text{Sb}_{2-x}\text{Fe}_x\text{Te}_3$. a) The undoped Sb_2Te_3 cell is characterized by a large Sb-Te bond distance $d=3.18 \text{ \AA}$. The shaded area indicates the valence electron density. b) The Fermi surface calculated for p-type Sb_2Te_3 viewed along the (001) projection includes of six major ellipsoids from the hole bands. For comparison, the red ellipsoid depicts an area of 0.405 nm^2 . c) The Fe dopant (black) causes a crystallographic distortion in the Sb_2Te_3 supercell and yields a reduced cation-anion distance $d=2.84 \text{ \AA}$ with an enhanced electron density near the Fe. d) The inner Fermi surface for the $\text{Sb}_{2-x}\text{Fe}_x\text{Te}_3$ includes an additional pocket at the Γ point. The cross-sectional area of the two highlighted features are 0.72 and 1.98 nm^2 respectively. e) The exchange-splitting forms a second Fermi surface (right) that wraps the inner $\text{Sb}_{2-x}\text{Fe}_x\text{Te}_3$ surface. e) The band structure of pure Sb_2Te_3 indicates a predominant s-p character and shows the light and heavy hole bands at the Fermi surface. The green line is the energy used to draw the Fermi surface. f) The band-structure of the $\text{Sb}_{2-x}\text{Fe}_x\text{Te}_3$ shows an additional hole band at Γ at the valence band.

To clarify the topology of the Fermi surface features detected in the sDH oscillations, density functional theory calculations were performed. Fig. 6 summarizes the DFT calculations comparing pure Sb_2Te_3 with $\text{Sb}_{2-x}\text{Fe}_x\text{Te}_3$. The undistorted crystal structure of Sb_2Te_3 is shown in Fig. 6a. The corresponding Fermi surface is shown in Fig. 6 b,

where p-type doping has been modelled by shifting the Fermi surface to $E = -0.1$ eV. The Fermi surface viewed along the k_z projection consists of six ellipsoidal valence bands derived from the hole bands along six-fold symmetric $\Gamma \rightarrow M$ lines. This agrees with past work which proposed a six ellipsoid valence band model of Sb_2Te_3 . [24-26] At moderate doping corresponding to $E_F = -0.1$ eV, the maximum cross-sectional area of these light-hole ellipsoids is 0.405 nm^2 in reasonable agreement with experimental signature in the sdH oscillations (0.48 nm^2). Heavier p-type doping results in a further six heavy-hole pockets becoming populated. The offset between the valence band maxima (VBM) is very sensitive to strain and external pressure in Sb_2Te_3 . [27, 28]

The Fe dopant introduces a local crystallographic distortion in the Sb_2Te_3 cell that is reflected in the band structure. Figure 6 c shows the relaxed chemical structure of a supercell containing a Fe-dopant and indicates that Fe-Te bond-lengths ($d_{\text{Fe-Te}} = 2.87 \text{ \AA}$) are shorter than the analogous Sb-Te bond-lengths ($d_{\text{Sb-Te}} = 3.18 \text{ \AA}$). Fig. 6 d shows the Fermi surface after Fe-doping. The joint effect of hole-doping and distortion introduced by the Fe modifies the valence band maxima (VBM) features and consequently, the Fermi surface in the $\text{Sb}_{2-x}\text{Fe}_x\text{Te}_3$ has additional features, most prominently at the Γ point. The cross-sectional area of the closed orbits of the ellipsoids is expanded in the Fe-doping to 1.98 nm^2 whereas the Γ pocket has a smaller area corresponding to 0.7 nm^2 . These can be tentatively assigned to the larger and smaller sdH oscillation frequency. Exchange splitting also gives rise to a second larger Fermi surface (Fig. 7 e) which contains open orbitals, making it unlikely to contribute to the sdH oscillations.

The band-structure of the undoped Sb_2Te_3 (Figure 6 f) and Fe-doped Sb_2Te_3 (Figure 6g) clearly show the contrasting features in the VBM at the Γ and M points which are responsible for the respective Fermi surface. By analyzing the band-character, it is seen that the Γ point in Fe-doped Sb_2Te_3 is comprised entirely of Sb-Te s-p orbitals, and therefore hybridization with the Fe d levels does not play a direct role. Instead, this band energy is a reflection of the crystallographic distortion and strain introduced by the dopant.

4. Conclusions

With Fe doping, the Sb_2Te_3 single crystal still possesses a metallic state with a large MR in low temperature region. Compared with Sb_2Te_3 , FST shows more complexity in its Fermi surface morphology, which manifests as multi-frequency oscillation patterns in MR measurements. In the angular-dependent measurement, the oscillation frequencies shift, and two of the frequencies indicate 2D-like behavior. We tentatively assign these two features to the two-valence band minimum, one of which is intrinsic to Sb_2Te_3 , and one which is introduced by chemical strain associated with the Fe dopant. Further, we find that both samples are hole-carrier dominated, and Fe doping reduces the carrier's density, and mobility. These results show that the hybridization of transition-metal defect bands with the intrinsic Sb_2Te_3 bands is a crucial consideration if such materials are to be incorporated into future electronic devices.

5. Acknowledgements

We acknowledge support from the ARC Professional Future Fellowship (FT130100778), DP130102956, DP170104116, DP170101467 and ARC Centre of Excellence in Future Low-Energy Electronics Technologies. This research was undertaken with the assistance of resources and services from the National Computational Infrastructure (NCI), which is supported by the Australian Government.

[1] B.A. Bernevig, T.L. Hughes, S.-C. Zhang, Quantum spin Hall effect and topological phase transition in HgTe quantum wells, *Science*, 314 (2006) 1757-1761.

[2] M.Z. Hasan, C.L. Kane, Colloquium: topological insulators, *Reviews of Modern Physics*, 82 (2010) 3045.

[3] X.-L. Qi, S.-C. Zhang, Topological insulators and superconductors, *Reviews of Modern Physics*, 83 (2011) 1057.

[4] X. Wang, Y. Du, S. Dou, C. Zhang, Room temperature giant and linear magnetoresistance in

- topological insulator Bi_2Te_3 nanosheets, *Physical review letters*, 108 (2012) 266806.
- [5] R. Yu, W. Zhang, H.-J. Zhang, S.-C. Zhang, X. Dai, Z. Fang, Quantized anomalous Hall effect in magnetic topological insulators, *Science*, 329 (2010) 61-64.
- [6] C.-Z. Chang, J. Zhang, X. Feng, J. Shen, Z. Zhang, M. Guo, K. Li, Y. Ou, P. Wei, L.-L. Wang, Experimental observation of the quantum anomalous Hall effect in a magnetic topological insulator, *Science*, 340 (2013) 167-170.
- [7] Z. Zhou, Y.-J. Chien, C. Uher, Thin film dilute ferromagnetic semiconductors $\text{Sb}_{2-x}\text{Cr}_x\text{Te}_3$ with a Curie temperature up to 190 K, *Physical Review B*, 74 (2006) 224418.
- [8] L. Collins-McIntyre, L. Duffy, A. Singh, N.-J. Steinke, C. Kinane, T. Charlton, A. Pushp, A. Kellock, S. Parkin, S. Holmes, Structural, electronic, and magnetic investigation of magnetic ordering in MBE-grown $\text{Cr}_x\text{Sb}_{2-x}\text{Te}_3$ thin films, *EPL (Europhysics Letters)*, 115 (2016) 27006.
- [9] S. Gupta, S. Kanai, F. Matsukura, H. Ohno, Magnetic and transport properties of Sb_2Te_3 doped with high concentration of Cr, *Applied Physics Express*, 10 (2017) 103001.
- [10] P. Sessi, R.R. Biswas, T. Bathon, O. Storz, S. Wilfert, A. Barla, K.A. Kokh, O.E. Tereshchenko, K. Fauth, M. Bode, Dual nature of magnetic dopants and competing trends in topological insulators, *Nature communications*, 7 (2016).
- [11] H.-J. Kim, K.-S. Kim, J.-F. Wang, V. Kulbachinskii, K. Ogawa, M. Sasaki, A. Ohnishi, M. Kitaura, Y.-Y. Wu, L. Li, Topological Phase Transitions Driven by Magnetic Phase Transitions in $\text{Fe}_x\text{Bi}_{2-x}\text{Te}_3$ ($0 \leq x \leq 0.1$) Single Crystals, *Physical review letters*, 110 (2013) 136601.
- [12] Y.S. Hor, P. Roushan, H. Beidenkopf, J. Seo, D. Qu, J.G. Checkelsky, L.A. Wray, D. Hsieh, Y. Xia, S.-Y. Xu, Development of ferromagnetism in the doped topological insulator $\text{Bi}_{2-x}\text{Mn}_x\text{Te}_3$, *Physical Review B*, 81 (2010) 195203.
- [13] P. Haazen, J.-B. Laloë, T. Nummy, H. Swagten, P. Jarillo-Herrero, D. Heiman, J. Moodera, Ferromagnetism in thin-film Cr-doped topological insulator Bi_2Se_3 , *Applied Physics Letters*, 100 (2012) 082404.
- [14] A. Panfilov, G. Grechnev, A. Fedorchenko, K. Conder, E. Pomjakushina, Magnetic properties of Mn-doped Bi_2Se_3 compound: temperature dependence and pressure effects, *Journal of Physics: Condensed Matter*, 27 (2015) 456002.
- [15] W.M. Haynes, *CRC handbook of chemistry and physics*, CRC press 2014.
- [16] L. Zhao, H. Deng, I. Korzhovska, M. Begliarbekov, Z. Chen, E. Andrade, E. Rosenthal, A. Pasupathy, V. Oganessian, L. Krusin-Elbaum, Emergent surface superconductivity in the topological insulator Sb_2Te_3 , *Nature communications*, 6 (2015) 8279.
- [17] J.-M. Zhang, W. Ming, Z. Huang, G.-B. Liu, X. Kou, Y. Fan, K.L. Wang, Y. Yao, Stability, electronic, and magnetic properties of the magnetically doped topological insulators Bi_2Se_3 , Bi_2Te_3 , and Sb_2Te_3 , *Physical Review B*, 88 (2013) 235131.
- [18] G. Kresse, Software vasp, vienna, 1999; g. kresse, j. furthmüller, *Phys. Rev. B*, 54 (1996) 169.
- [19] G. Kresse, D. Joubert, From ultrasoft pseudopotentials to the projector augmented-wave method, *Physical Review B*, 59 (1999) 1758.
- [20] S. Grimme, J. Antony, S. Ehrlich, H. Krieg, A consistent and accurate ab initio parametrization of density functional dispersion correction (DFT-D) for the 94 elements H-Pu, *The Journal of chemical physics*, 132 (2010) 154104.
- [21] Y. Jiang, Y. Wang, M. Chen, Z. Li, C. Song, K. He, L. Wang, X. Chen, X. Ma, Q.-K. Xue, Landau quantization and the thickness limit of topological insulator thin films of Sb_2Te_3 , *Physical review letters*,

108 (2012) 016401.

[22] V. Kulbachinskii, A. Kudryashov, V. Kytin, The Shubnikov-de Haas effect and thermoelectric properties of TI-doped Sb_2Te_3 and Bi_2Te_3 , *Semiconductors*, 49 (2015) 767-773.

[23] D. Shoenberg, *Magnetic Oscillations in Metals* Cambridge Univ, Press, Cambridge, DOI (1984).

[24] V. Kulbachinskii, Z.M. Dashevskii, M. Inoue, M. Sasaki, H. Negishi, W. Gao, P. Lostak, J. Horak, A. De Visser, Valence-band changes in $\text{Sb}_{2-x}\text{In}_x\text{Te}_3$ and $\text{Sb}_2\text{Te}_{3-y}\text{Se}_y$ by transport and Shubnikov-de Haas effect measurements, *Physical Review B*, 52 (1995) 10915.

[25] A. Von Middendorff, K. Dietrich, G. Landwehr, Shubnikov-de haas effect in p-type Sb_2Te_3 , *Solid State Communications*, 13 (1973) 443-446.

[26] H. Köhler, A. Freudenberger, Investigation of the highest valence band in $(\text{Bi}_{1-x}\text{Sb}_x)_2\text{Te}_3$ crystals, *physica status solidi (b)*, 84 (1977) 195-203.

[27] B.Y. Yavorsky, N. Hinsche, I. Mertig, P. Zahn, Electronic structure and transport anisotropy of Bi_2Te_3 and Sb_2Te_3 , *Physical Review B*, 84 (2011) 165208.

[28] J. Zhu, J. Zhang, P. Kong, S. Zhang, X. Yu, J. Zhu, Q. Liu, X. Li, R. Yu, R. Ahuja, Superconductivity in topological insulator Sb_2Te_3 induced by pressure, *Scientific reports*, 3 (2013) 2016.